ANL-80-72

L-80-72

NEUTRON-INDUCED HELIUM IMPLANTATION IN GCFR CLADDING

by

H. Yamada, R. B. Poeppel,
and R. H. Sevy

ARGONNE NATIONAL LABORATORY

ARGONNE NATIONAL LABORATORY, ARGONNE, ILLINOIS

Prepared for the U. S. DEPARTMENT OF ENERGY
under Contract W-31-109-Eng-38

DISCLAIMER

Printed in the United States of America
Available from
National Technical Information Service
U. S. Department of Commerce
5285 Port Royal Road
Springfield, VA 22161

NTIS price codes
Printed copy: A03
Microfiche copy: A01

Distribution Category:
Gas Cooled Reactor Technology
(UC-77)

ANL-80-72

ARGONNE NATIONAL LABORATORY
9700 South Cass Avenue
Argonne, Illinois 60439

NEUTRON-INDUCED HELIUM IMPLANTATION IN GCFR CLADDING

by

H. Yamada and R. B. Poeppel
Materials Science Division

and

R. H. Sevy
Reactor Analysis and Safety Division

October 1980

THIS PAGE

WAS INTENTIONALLY

LEFT BLANK

TABLE OF CONTENTS

LIST OF FIGURES

LIST OF TABLES

NEUTRON-INDUCED HELIUM IMPLANTATION IN GCFR CLADDING

by

H. Yamada, R. B. Poeppel, and R. H. Sevy

ABSTRACT

The neutron-induced implantation of helium atoms on the exterior surfaces of the cladding of a prototypic gas-cooled fast reactor (GCFR) has been investigated analytically. A flux of recoil helium particles as high as 4.2×10^{10} He/cm^2·s at the cladding surface has been calculated at the peak power location in the core of a 300-MWe GCFR. The calculated profile of the helium implantation rates indicates that although some helium is implanted as deep as 20 μm, more than 99% of helium particles are implanted in the first 2-μm-deep layer below the cladding surface. Therefore, the implanted helium particles should mainly affect surface properties of the GCFR cladding.

I. INTRODUCTION

The neutron-induced implantation of helium atoms was first reported by Gaus et al.[1] in silver targets during irradiations in a thermal reactor. Without performing a detailed analysis of the implantation processes, they obtained reasonable agreement between experimentally observed and calculated helium concentrations. Subsequently, Altenhein et al.[2] performed a similar analysis with structural materials for fusion-reactor blankets. They concluded that the helium implantation might destroy the thin surface coatings that were thought necessary to protect refractory metals against oxygen and other interstitial contaminants.

Recent gas-cooled fast reactor (GCFR) designs[3] use high-pressure (89 atm; 8.9 MPa) helium gas as the proposed coolant medium. Therefore, it is expected that a significant amount of helium will be implanted in the structural materials in the core of the GCFR. Hence, in this paper an attempt has been made to obtain an estimate of the helium implantation rate on the exterior surfaces of the GCFR cladding.

II. THEORY

The neutron-induced implantation of helium atoms is schematically illustrated in Fig. 1. A neutron with energy E collides elastically with a helium atom and transfers energy E_a to the helium atom. The recoil helium

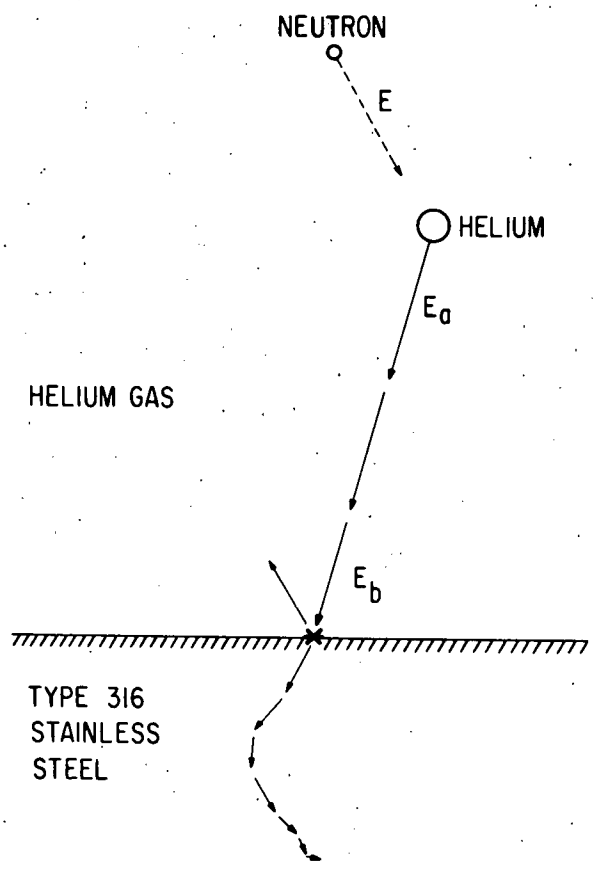

Fig. 1. Schematic Illustration of Neutron-induced Helium Implantation in GCFR Cladding.

particle will lose energy as it travels through the helium gas coolant, reaching the cladding surface with energy E_b. This energy loss is mainly due to electronic stopping in the energy range of interest. Therefore, we can assume that energetic recoil helium particles will lose energy continuously and maintain their original recoil directions. At the cladding surface, some recoil helium particles will be reflected back into the gas while the remainder will penetrate through the cladding surface and come to rest after multiple collisions in the cladding material. These collisions deflect the helium particles from their original recoil directions. Hence, a Monte Carlo method was used for calculation of the depth distribution.

III. NUMERICAL CALCULATIONS

The flux of recoil helium particles at the cladding surface can be estimated by summing the contributions of all neutron-helium collisions in the volume of helium gas surrounding the cladding surface.

1. Neutron Spectrum

The neutron-flux distribution $\Psi(E)$ employed in the present calculation was reported by Wei.[4] Wei has evaluated the flux at the peak-power location in the core of a prototypic 300-MWe GCFR. He reported the results as fluxes in 11 energy intervals. In order to facilitate numerical integration, we have redefined the neutron-flux distribution over a greater number of energy intervals. The neutron energies between 1 keV and 10 MeV were partitioned into four energy intervals; 1 to 10 keV, 10 to 100 keV, 100 to 1000 keV, and 1 to 10 MeV. Each energy interval was partitioned further into nine equal energy subintervals. The fast-neutron fluxes in these 36 energy subintervals were determined from a Weibull distribution[5] fit to the distribution reported by Wei. This representation of the neutron-flux distribution is shown in Fig. 2.

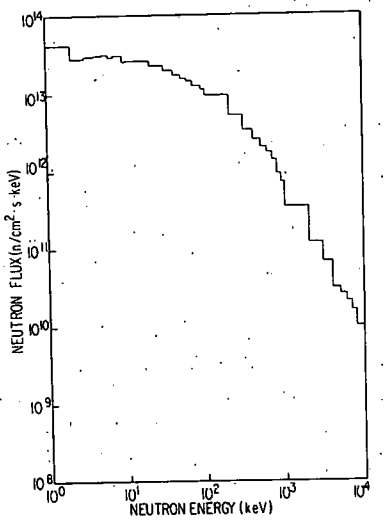

Fig. 2. A 36-energy-interval Representation of the Neutron-flux Spectrum Reported by Wei (Ref. 4).

2. Primary-recoil Helium

The number of primary-recoil helium particles produced in the helium gas is determined simply by integrating the product of the neutron flux, the density of helium atoms, and the scattering cross section over the neutron-flux spectrum.

The number $N(E_a)dE_a$ of primary-recoil helium particles produced with energies between E_a and $E_a + dE_a$ in a unit volume of the helium gas per unit time is given by

$$N(E_a)dE_a = \int \Psi(E)dE\ \sigma(E,E_a)dE_a\ \rho(P,T)\ , \qquad (1)$$

where $\Psi(E)dE$ is the flux of neutrons with energies between E and E + dE, and $\rho(P,T)$ is the number of helium atoms per unit volume in helium gas at pressure P and temperature T. The differential scattering cross section $\sigma(E,E_a)$ is given by

$$\sigma(E,E_a) = \begin{cases} \sigma(\theta')\ 4\pi/(E_a)_{max}, & 0 \leq E_a \leq (E_a)_{max} \\ 0, & E_a > (E_a)_{max} \end{cases} \qquad (2)$$

where $\sigma(\theta')$, the differential scattering cross section in the center-of-mass system, is a function of the collision angle θ'.* The quantity $(E_a)_{max}$ is the maximum energy that can be transferred to a recoil helium particle in a neutron-helium collision and is equal to 0.64E for the neutron-helium (^{4}He) collision.

Since natural helium contains only 0.00013% of ^{3}He, we can simplify the calculations by neglecting the $^3_2$He (n,P) $^3_1$H reaction by which neutrons are lost, and considering only elastic scattering. Pennington[6] has calculated the elastic scattering cross section and Legendre expansion coefficients from s-, p-, and d-wave phase shifts. We have used his results, compiled in the ENDF/B-V format, for scattering of neutrons with energies between 1 keV and 10 MeV. We neglected the contribution from neutrons with energies < 1 keV and > 10 MeV because the flux becomes vanishingly small at these energies. The neutron scattering cross section of ^{4}He and the helium elastic scattering angular distributions are shown in Figs. 3 and 4, respectively.

Assuming a unique value of differential scattering cross section corresponding to the fast-neutron energy in the middle of each energy subinterval, we calculated the number of recoil helium particles produced in a unit volume of helium gas per unit time as a function of recoil energy E_a. The resulting recoil helium distribution $N(E_a)$ is shown in Fig. 5. We used the same energy intervals to define the recoil-helium energy distribution as we used for the fast-neutron flux spectrum. As shown in Fig. 5, $N(E_a)$ decreases from 10^{11} He/cm^3·s·keV at E_a = 1 keV to 10^5 He/cm^3·s·keV at E_a = 7 MeV.

3. Stopping Power

Before energetic helium particles can strike the stainless steel surfaces, they must travel some distance through the helium gas and some of their energy will be lost. The energy loss of energetic helium particles has been widely investigated[7] and reported in terms of the stopping power. The stopping power S_p is defined by

$$S_p = \frac{dE}{dr}\ , \qquad (3)$$

---

*For the definition of the collision angle θ', see, for example, p. 16 of Ref. 7.

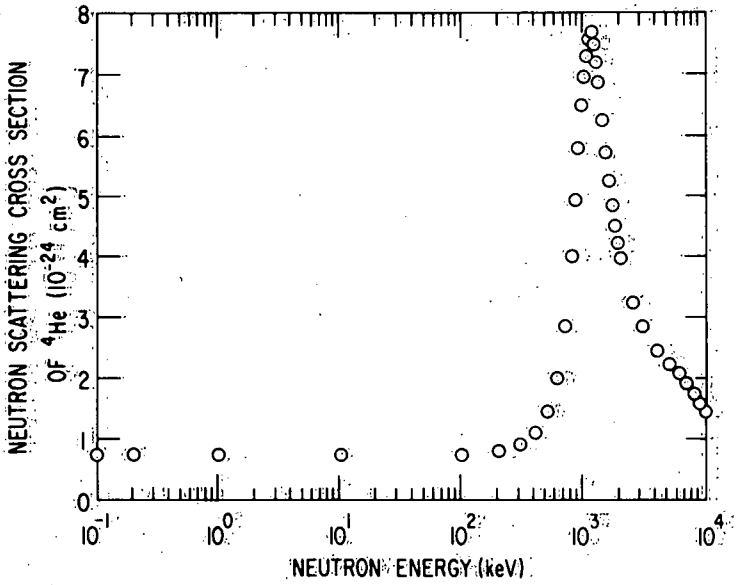

Fig. 3. Helium Elastic Scattering Cross Section as a Function of Neutron Energy.

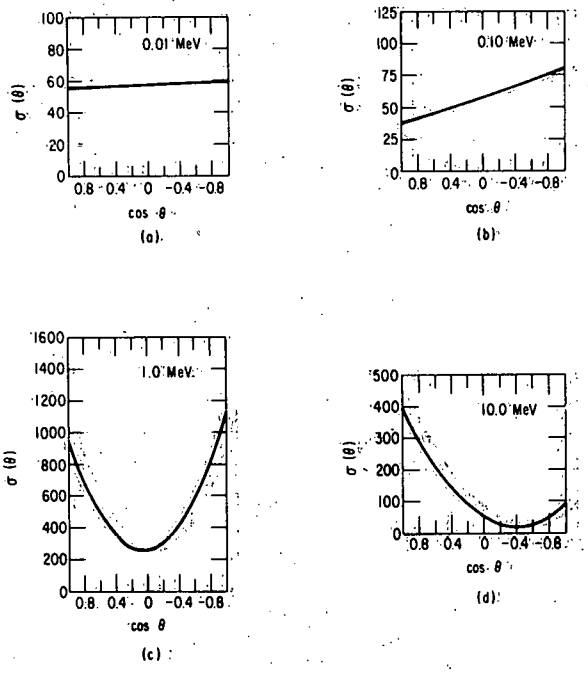

Fig. 4. Helium Elastic Scattering Angular Distributions for Neutron Energies of (a) 0.01, (b) 0.10, (c) 1.0, and (d) 10.0 MeV. $\sigma(\theta)$ is in units of 10^{-27} cm^2/steradian.

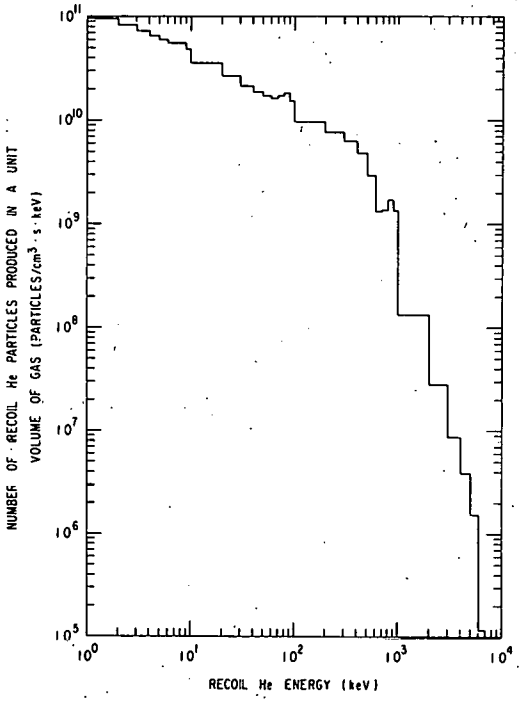

Fig. 5. Number of Recoil Helium Particles Produced by Elastic Scattering of Fast Neutrons as a Function of Recoil Energy, E_a.

where dE is the amount of kinetic energy lost while traveling a distance dr. Values of the stopping power of gaseous helium were obtained from Ziegler[8] and are shown in Fig. 6.

The energy E_b of the recoil helium particles at the cladding surface is related to the original recoil energy E_a and the distance r the particles travel through the helium gas via

$$r = \int_{E_a}^{E_b} \frac{dE}{S_p'(\rho,E)} , \tag{4}$$

where $S_p'(\rho,E)$ is the modified stopping power used for the projected-range calculation. It is a function of the density ρ of helium gas and the energy E of the helium particle.

4. Helium Particle Flux at the Cladding Surface

The calculation of the helium particle flux at the cladding surface can be reduced to a geometrical integration (Fig. 7). The flux of recoil helium particles $M(E_b)dE_bdA$ passing through an area dA of the cladding surface with energies between E_b and $E_b + dE_b$, and with recoil energies between E_a and $E_a + dE_a$ produced by neutron-helium collisions at distances between

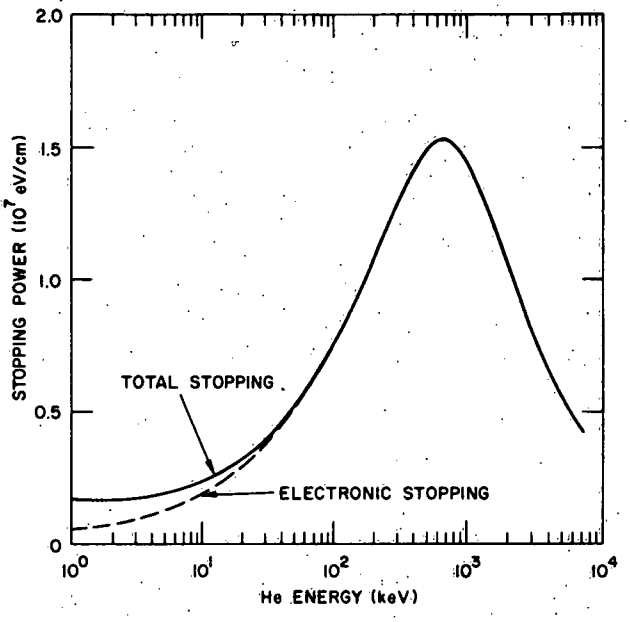

Fig. 6. Stopping Power of Gaseous Helium under Conditions Prototypic of the 300-MWe GCFR (Pressure = 8.9 MPa, Temperature = 550°C).

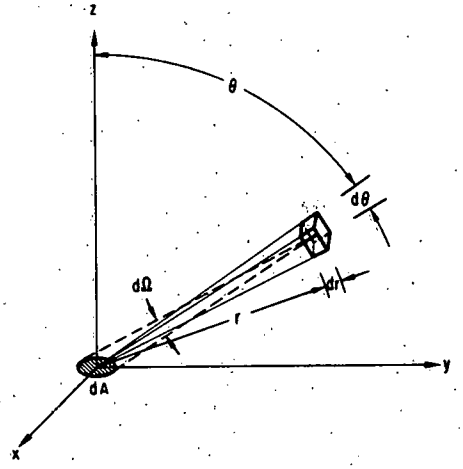

Fig. 7. Geometry Used to Derive Eq. (5), the Flux of Recoil Helium Particles at the Surface of the Cladding.

r and r + dr from dA, is obtained by integration over a spherical shell:

$$M(E_b)dE_b dA = \int \alpha(E_b,\theta)(2\pi r \sin\theta)(rd\theta dr)N(E_a)dE_a \frac{d\Omega}{4\pi} . \quad (5)$$

The angle of incidence is θ, and $d\Omega$ is the solid angle at the point of primary recoil subtended by dA:

$$d\Omega = \frac{dA \cos\theta}{r^2} . \quad (6)$$

The probability that an incident helium particle is implanted in the cladding and not reflected back into the helium coolant is denoted by $\alpha(E_b,\theta)$.

5. Implantation Probability

The implantation probability $\alpha(E_b,\theta)$ for helium in stainless steel has not been determined experimentally. A Monte Carlo computer program which was originally formulated by Biersack[9] to simulate slowing down and scattering of energetic ions in amorphous targets was used to evaluate $\alpha(E_b,\theta)$ in the energy range of interest. The computer program follows a large number of individual ion or particle "histories" in a target. Each history begins with a given energy, position, and direction. The particle is assumed to change direction as a result of binary nuclear collisions and to move in straight free-flight paths between collisions. The energy is reduced as a result of nuclear and electronic energy losses, and a history is terminated when the energy drops below a prespecified value. The target is considered amorphous, with atoms at random locations, and thus the directional properties of the crystal lattice are ignored. The nuclear and electronic energy losses or stopping powers are assumed to be independent of each other. Thus particles lose energy in discrete amounts in nuclear collisions, and lose energy continuously from electronic interactions. The formalism incorporated into the computer program has been found to be applicable to a large variety of ion-target combinations, including helium-niobium and helium-copper combinations.[9]

In our calculation, we treated Type 316 stainless steel GCFR cladding as an amorphous mixture of Fe, Ni, Cr, and minor constituents. The calculated probability $\alpha(E_b,\theta)$ of implantation of energetic helium particles in the cladding is shown in Fig. 8 as a function of incident angle θ, for five values of incident energy E_b. The Monte Carlo calculation was performed for each of nine values of θ. The result of each calculation is based on 10^3 particle histories. In order to determine whether 10^3 is a sufficient number of histories, we repeated the calculation using 5×10^3 and again using 10^4 histories for an incident helium particle energy of 100 keV. The results were almost identical with those shown in Fig. 8. Therefore, 10^3 particle histories seem sufficient.

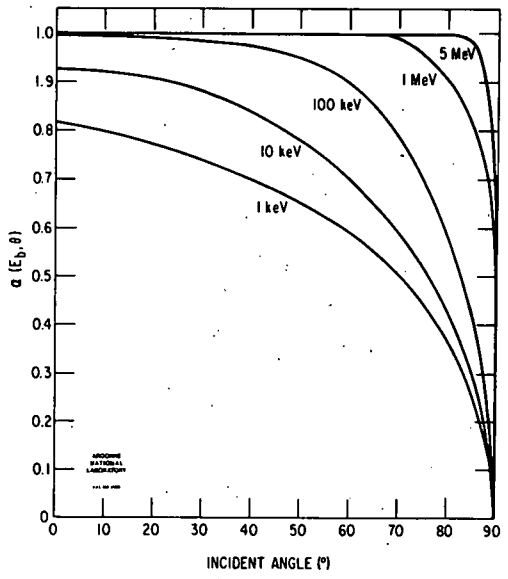

Fig. 8. Probability of Implantation of Energetic Helium Particles in Type 316 Stainless Steel as a Function of Incident Angle, for Five Values of Incident Energy.

6. Projected Range of Implanted Helium Particles

The initial distribution of implanted helium in the cladding can be defined by the projected range and the standard deviation in the projected range. Helium can diffuse in the cladding and precipitate as helium bubbles. In the present paper, we will be concerned with the initial distribution only. Given this distribution, we may conjecture about the probable ultimate fate of the helium and the cladding.

Since the projected ranges and standard deviations of helium particles in solids are typically in the range of 100 Å to 100 μm,[8] the helium implantation rate, which is generally a function of three Cartesian coordinates x, y, and z in the solid, can be averaged over a large surface area of the solid and represented approximately by a function of only one coordinate, z, the distance normal to the surface of the solid. The helium implantation rate I(z) within the cladding can then be given by

$$I(z)dz = \int_{E_b,\theta} m(E_b,\theta)dE_b d\theta\ K(E_b,\theta,z)dz\ , \qquad (7)$$

where $m(E_b,\theta)$ is an angular distribution function of the flux of incident recoil helium particles with energy E_b, and $K(E_b,\theta,z)$ is an implantation distribution function. Since the ion implantation distribution is roughly Gaussian, this shape is used as an approximation in the calculation. Assuming a Gaussian distribution, the implantation distribution function

$K(E_b,\theta,z)$ is given by

$$K(E_b,\theta,z) = \frac{1}{(2\pi)^{1/2} D(E_b,\theta)} \exp\left\{ - \frac{[z - z_o(E_b,\theta)]^2}{2D(E_b,\theta)} \right\}, \qquad (8)$$

where $z_o(E_b,\theta)$ and $D(E_b,\theta)$ are the projected range and standard deviation, respectively. The calculated values are shown in Fig. 9 as a function of the incident angle for five values of incident energy. Again, the result of each calculation is based on 10^3 particle histories. The projected range shows a significant deviation from a simple cosine dependence for low-energy particles. Since the first few nuclear collisions tend to randomize the direction of the particle, those particles which stay in the solid come to rest with a depth distribution independent of the original incident angle.

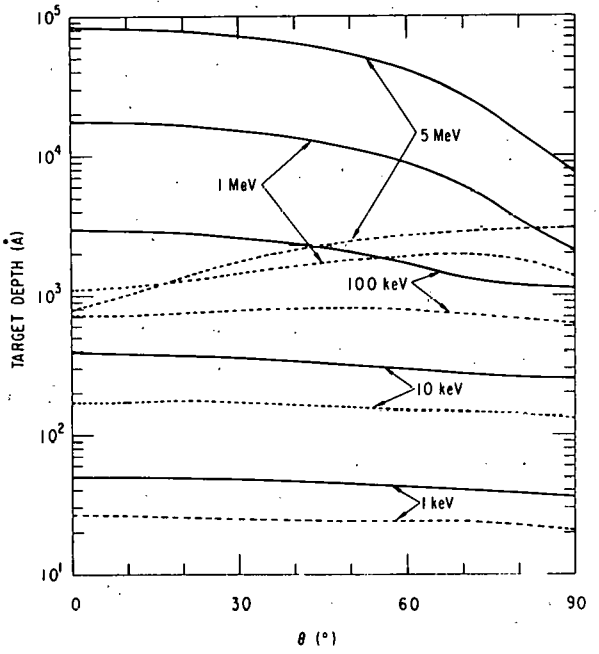

Fig. 9. Projected Ranges (Solid Curves) and Standard Deviations (Dashed Curves) of Implanted Helium Particles in Type 316 Stainless Steel for Five Values of Incident Energy.

IV. RESULTS

The expected helium implantation in fuel-element cladding of a prototypic GCFR was calculated. The calculated number of recoil helium particles produced in the helium gas at 550°C and 89 atm (8.9 MPa) is 6.4×10^{12} He/cm^3·s for $E_a > 1$ keV. The coolant-channel geometry is shown in Fig. 10. The minimum dimension of the channel is 0.254 cm (0.100 in.). As a first approximation, the integration in Eq. (5) was carried out numerically for the distance r from 0 to 0.254 cm. The calculated flux of recoil helium particles at the cladding surface is shown in Fig. 11 as a function of incident energy. The flux decreases from 7×10^8 to 4×10^4 He/cm^2·s·keV as the incident helium energy increases from 1 keV to 6 MeV. The integrated flux is 5.6×10^{10} He/cm^2·s for $E_b > 1$ keV.

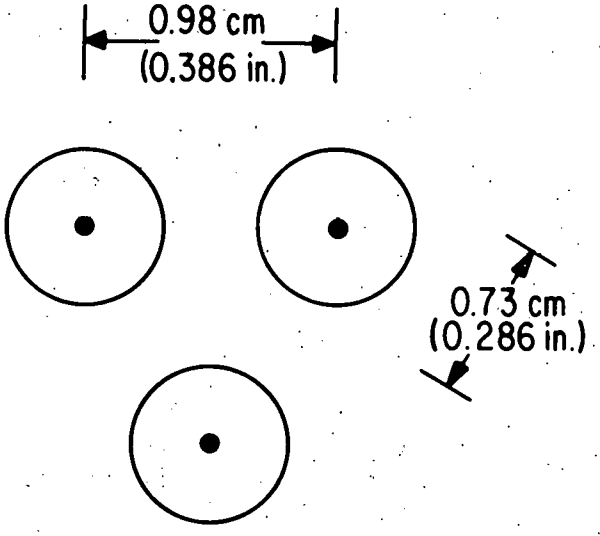

Fig. 10. GCFR Fuel-rod Arrangement (General Atomic design).

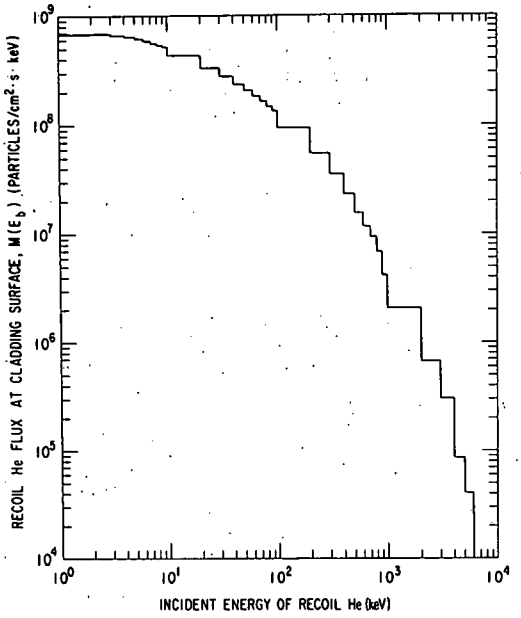

Fig. 11. Flux of Recoil Helium Particles at the Cladding Surface as a Function of Incident Energy E_b.

Since a significant fraction of the stopping power of gaseous helium for E < 30 keV is due to nuclear scattering (Fig. 6), the assumption of very little angular deflection of recoil helium particles is no longer valid for recoil energies < 30 keV. Hence, it is expected that some of the recoil helium particles will be deflected significantly from the original recoil angles and will never reach the cladding surface. Instead of treating these nuclear scatterings of energetic helium particles by helium atoms precisely, by employing a Monte Carlo type simulation method, the flux of recoil helium particles was integrated for recoil helium energies > 30 keV. The recoil rate of helium with E_a > 30 keV is 5.2×10^{12} He/cm^3·s and the integrated flux for E_b > 30 keV is 4.2×10^{10} He/cm^2·s. The flux is about 75% of that calculated for E_b > 1 keV. Hence, no further attempt was made to assess the effect of the nuclear scattering of energetic recoil helium particles on the flux of recoil helium particles.

In order to investigate the radial variation of the flux of the recoil helium particles around the outer surface of the GCFR cladding, the integration in Eq. (5) was carried out for a distance r up to 1 cm, which corresponds to the projected range of recoil helium particles with energy of 7 MeV. The integrated fluxes for E_b > 1 keV and E_b > 30 keV are found to be 5.6×10^{10} and 4.3×10^{10} He/cm^2·s, respectively, which are very close to those calculated for r = 0.254 cm. Since very few recoil helium particles with recoil energy larger than 7 MeV are produced in the core of the GCFR, the integration of Eq. (5) using larger values of r will not contribute any further increases in the integrated flux of recoil helium particles at the cladding surface. Therefore, the integrated flux of

4.2×10^{10} He/cm^2·s (E_b > 30 keV) is the maximum value anticipated at the cladding surface of the GCFR. The radial variation of the flux of recoil helium particles around the outer surface of the GCFR cladding is expected to be very small. The results of these calculations are summarized in Table I.

Table I. Total Number of Recoil Helium Particles Produced per cm^3·s and the Total Recoil Helium Flux at the Cladding Surface in a Prototypic 300-MWe GCFR

		E > 1 keV	E > 30 keV
Total Recoil Helium Particles, $\int_E^\infty N(E_a)dE_a$, He/cm^3·s		6.38×10^{12}	5.16×10^{12}
Total Recoil Helium Flux at the Cladding Surface, $\int_E^\infty M(E_b)dE_b$, He/cm^2·s	r_{max} = 0.254 cm	5.55×10^{10}	4.23×10^{10}
	r_{max} = 1.0 cm	5.64×10^{10}	4.32×10^{10}

The depth distribution was calculated using Eq. (7). To evaluate Eq. (7) numerically, $m(E_b,\theta)\Delta E_b \Delta\theta$ was first calculated for incident angles ranging from 0 to 90° (in 10° increments) for a given energy range. Then, with the assumption of a unique projected range and standard deviation corresponding to each combination of incident angle and recoil energy range, the helium implantation rates were calculated every 0.1 μm for penetration depths up to 25 μm by summing every contribution from all possible combinations of the incident angle and recoil energy. The results are shown in Fig. 12. In the figure, two implantation rates based on the integrated fluxes of recoil helium particles with E_b > 30 keV and E_b > 1 keV are presented. Since not all of the recoil helium particles with recoil energies between 1 keV and 30 keV are expected to be deflected away from the cladding surface, it is not obvious whether the peak of helium implantation rate just beneath the cladding surface is real. Although 99% of recoil helium particles are implanted in the first 2-μm-deep layer of the GCFR cladding, substantial helium implantation is expected in the first 20-μm-deep layer of the cladding. Beyond a depth of 20 μm, the helium concentration is expected to be constant and primarily due to (n,α) reactions of major constituents of the cladding alloy. Although it is beyond the scope of this paper to

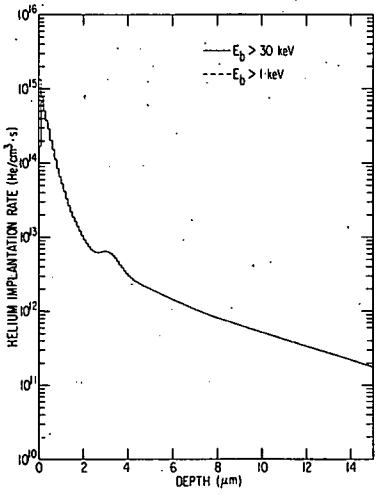

Fig. 12. Helium Implantation Rate in GCFR Cladding as a Function of Penetration Depth.

calculate time-dependent variations of helium profiles in GCFR cladding, it is expected that the helium profile shown in Fig. 12 can be linearly extrapolated with time, up to the time when helium bubble or blister formation begins.

V. DISCUSSION

The results presented in this paper may be compared with an experimentally observed helium concentration in 20% cold-worked Type 316 stainless-steel cladding reported by Farrar et al.[10] Their specimen was an unfueled cladding tube pressurized by 121 atm (12.1 MPa) of helium gas and irradiated in the Experimental Breeder Reactor II (EBR-II) at 577°C with a fast-neutron fluence of up to 0.43×10^{22} n/cm^2 (E > 0.1 MeV). The measured helium concentration, averaged over the entire wall thickness, was 7.85 ± 0.65 appm. Since a helium concentration of only 0.77 appm was reported to be produced by (n,α) reactions in the stainless steel,[10] a helium concentration of 7.08 appm can be attributed to neutron-induced helium implantation. Employing the spectrum of fast-neutron fluxes present in subassembly X157 of EBR-II, in which the cladding tube was irradiated, we calculated an average helium concentration of 13.1 appm over the entire wall thickness of the cladding tube, which is less than a factor of 2 higher than that measured. Since a very large fraction of the total implanted helium is expected just beneath the surface, any surface pretreatment similar to the one reported by Farrar et al. might affect the helium measurement. Therefore, the agreement between the measurement and the calculation is remarkably good.

In exploring the possible consequences of helium implantation in GCFR cladding, it is appropriate to review here some phenomena attributed primarily to helium implantation. It is well known[11] that the implantation

of monoenergetic α-particles from particle accelerators causes formation of domeshaped blisters on surfaces of many materials including Type 316 stainless steel. Since the presence of a well-defined peak in the depth distribution of helium in the GCFR cladding is highly debatable, the accelerator evidence may not be relevant. However, McDonell has reported the formation of vertically elongated blisters on surfaces exposed to ^{252}Cf α-particles and fission fragments.[12] Although the helium profile generated by ^{252}Cf α-particles is very similar to the one calculated for the GCFR cladding, the large displacement damage caused by the fission fragments will not be present in the GCFR cladding.

Helium gas is known to encourage the development of microstructural damage in crystalline solids during displacive irradiation. For example, Farrell and Packan[13] reported that the introduction of simultaneously implanted helium at a rate of 20 appm He/dpa moves the swelling versus temperature curve up the temperature scale by 40 to 70 K in an annealed austenitic alloy (similar to Type 316 stainless steel) undergoing 4-MeV Ni^+ bombardment. In addition, helium gas is known to cause copious formation of grain-boundary cavities, boding ill for mechanical properties. For example, Bloom[14] reported significant reductions in both yield stress and total elongation for annealed Type 316 stainless steel irradiated in a mixed-spectrum reactor (high He appm/dpa ratio) compared with similar material irradiated in a fast reactor (low He appm/dpa ratio). Again, it is not at all clear how these changes in mechanical and swelling properties will affect the overall performance of the GCFR cladding, in which only a very shallow surface layer will be heavily implanted with helium gas.

VI. CONCLUSIONS

Implantation rates of energetic helium particles produced during elastic scattering of fast neutrons by helium atoms were calculated at the peak power location in the core of a 300-MWe GCFR. The calculated integrated flux of recoil helium particles at the GCFR cladding surface is 4.2×10^{10} He/cm^2·s (E_b > 30 keV). More than 99% of these helium particles are implanted in the first 2-μm-deep layer below the surface of the cladding. Hence, the implanted helium particles should produce mainly surface effects, such as blister formation. Although some helium is implanted at depths as great as 20 μm, the implanted helium is not expected to have drastic effects on the bulk properties of the GCFR cladding.

ACKNOWLEDGMENTS

The authors would like to express their sincere appreciation to M. Inokuti of ANL-RER for his helpful discussions concerning stopping power, and to J. P. Biersack of the Hahn-Meitner Institute, Berlin, West Germany, for permitting us to use his Monte Carlo computer program. E. M. Pennington of ANL-AP supplied the ENDF/B-V data on the helium differential scattering cross section, and T. Y. Wei of ANL-RAS supplied the fast-neutron flux distribution in the core of the GCFR.

REFERENCES

1. H. Gaus, H. Migge, and K. D. Mirus, Radiat. Eff. 18, 79 (1973).

2. F. K. Altenhein, H. Anderson, W. Lutze, G. Malow, and H. Migge, J. Nucl. Mater. 53, 332 (1974).

3. 300 MWe Gas-cooled Fast Breeder Reactor Demonstration Plant, General Atomic Company Report, GA-A13045 (1974).

4. T. Y. C. Wei, private communication.

5. For example, see N. L. Johnson and F. C. Leone, Statistics and Experimental Design in Engineering and the Physical Sciences, John Wiley and Sons (1976).

6. E. M. Pennington, ENDF/B Neutron Cross Section Data for Natural Helium, Argonne National Laboratory Report, ANL-7462 (1968).

7. For example, see Chr. Lehman, Interaction of Radiation with Solids and Elementary Defect Production, North-Holland Publishing Company (1977).

8. J. F. Ziegler, Helium: Stopping Powers and Ranges in All Elements, Pergamon Press (1977).

9. J. P. Biersack, private communication.

10. H. Farrar IV, Technical Progress Report - Fast Reactor Fluence Dosimetry, Atomic International Report, AI-ERDA-13181 (1976).

11. S. K. Das and M. Kaminsky, Radiation Blistering in Metals and Alloys, Radiation Effects on Solid Surfaces, M. Kaminsky, Ed. (Advance in Chemistry Series 158), American Chemical Society, Washington, D. C. (1976).

12. W. R. McDonell, Trans. Am. Nucl. Soc. 27, 271 (1977).

13. K. Farrell and N. H. Packan, J. Nucl. Mater. 85&86, 683 (1979).

14. E. E. Bloom, J. Nucl. Mater. 85&86, 795 (1979).

Distribution for ANL-80-72

Internal:

W. E. Massey
E. S. Beckjord
C. E. Till
R. Avery
L. Burris
D. W. Cissel
S. A. Davis
B. R. T. Frost
R. A. Lewis
L. G. LeSage
R. J. Teunis
R. S. Zeno
R. W. Weeks
W. J. Shack
R. B. Poeppel (5)
L. A. Neimark
H. Weidersich
S. Greenberg
F. A. Nichols
F. V. Nolfi
E. M. Stefanski (4)
G. R. Fenske
H. Yamada (10)
F. L. Yaggee
R. H. Sevy (5)
T. Y. Wei
D. Rose
J. T. Madell
C. E. Johnson
L. C. Walters
B. R. Seidel
D. L. Porter
E. L. Wood
A. B. Krisciunas
ANL Contract File
ANL Libraries (2)
TIS Files (6)

External:

DOE-TIC, for distribution per UC-77 (165)
Manager, Chicago Operations and Regional Office, DOE
Chief, Office of Patent Counsel, DOE-CORO
President, Argonne Universities Association
Materials Science Division Review Committee:
- E. A. Aitken, General Electric Co., Sunnyvale
- G. S. Ansell, Rensselaer Polytechnic Inst.
- A. Arrott, Simon Fraser U.
- R. W. Balluffi, Massachusetts Inst. Technology
- S. L. Cooper, U. Wisconsin
- C. Laird, U. Pennsylvania
- M. E. Shank, Pratt & Whitney, East Hartford
- C. T. Tomizuka, U. Arizona
- A. R. C. Westwood, Martin Marietta Labs.

E. Arbtin, EG&G Inc., Idaho Falls
D. Buttermer, Helium Breeder Associates, San Diego
H. Farrar, Rockwell International, Canoga Park
F. Garner, Hanford Engineering Development Lab.
R. B. Gordon, Helium Breeder Associates, San Diego
S. Langer, General Atomic Co.
H. Pearlman, Rockwell International, Canoga Park
R. Powel, Hanford Engineering Development Lab.
M. T. Simnad, General Atomic Co.
J. Straalsund, Hanford Engineering Development Lab.
A. Veca, General Atomic Co.
L. Welshans, Office of Nuclear Energy, USDOE
H. H. Yoshikawa, Hanford Engineering Development Lab.